RESEARCH

MADGAN: unsupervised Medical Anomaly Detection GAN using multiple adjacent brain MRI slice reconstruction

Changhee Han[1*], Leonardo Rundo[2,3], Kohei Murao[4], Tomoyuki Noguchi[5], Yuki Shimahara[1],
Zoltán Ádám Milacski[7], Saori Koshino[6], Evis Sala[2,3], Hideki Nakayama[8,9] and Shin'ichi Satoh[4]

*Correspondence: han@lpixel.net
[1]LPIXEL Inc., Tokyo, Japan
Full list of author information is
available at the end of the article

Abstract

Background: Unsupervised learning can discover various unseen abnormalities, relying on large-scale unannotated medical images of healthy subjects. Towards this, unsupervised methods reconstruct a 2D/3D single medical image to detect outliers either in the learned feature space or from high reconstruction loss. However, without considering continuity between multiple adjacent slices, they cannot directly discriminate diseases composed of the accumulation of subtle anatomical anomalies, such as Alzheimer's Disease (AD). Moreover, no study has shown how unsupervised anomaly detection is associated with either disease stages, various (i.e., more than two types of) diseases, or multi-sequence Magnetic Resonance Imaging (MRI) scans.

Results: We propose unsupervised Medical Anomaly Detection Generative Adversarial Network (MADGAN), a novel two-step method using GAN-based multiple adjacent brain MRI slice reconstruction to detect brain anomalies at different stages on multi-sequence structural MRI: (*Reconstruction*) Wasserstein loss with Gradient Penalty $+ 100 \, \ell_1$ loss—trained on 3 healthy brain axial MRI slices to reconstruct the next 3 ones—reconstructs unseen healthy/abnormal scans; (*Diagnosis*) Average ℓ_2 loss per scan discriminates them, comparing the ground truth/reconstructed slices. For training, we use two different datasets composed of $1,133$ healthy T1-weighted (T1) and 135 healthy contrast-enhanced T1 (T1c) brain MRI scans for detecting AD and brain metastases/various diseases, respectively. Our Self-Attention MADGAN can detect AD on T1 scans at a very early stage, Mild Cognitive Impairment (MCI), with Area Under the Curve (AUC) 0.727, and AD at a late stage with AUC 0.894, while detecting brain metastases on T1c scans with AUC 0.921.

Conclusions: Similar to physicians' way of performing a diagnosis, using massive healthy training data, our first multiple MRI slice reconstruction approach, MADGAN, can reliably predict the next 3 slices from the previous 3 ones only for unseen healthy images. As the first unsupervised various disease diagnosis, MADGAN can reliably detect the accumulation of subtle anatomical anomalies and hyper-intense enhancing lesions, such as (especially late-stage) AD and brain metastases on multi-sequence MRI scans.

Keywords: Generative adversarial networks; Self-attention; Unsupervised anomaly detection; Brain MRI reconstruction; Various disease diagnosis

Background

Machine Learning has revolutionized life science research, especially in Neuroimaging and Bioinformatics [1, 2], such as by modeling interactions between whole brain genomics/imaging [3, 4] and identifying Alzheimer's Disease (AD)-related proteins [5]. Especially, Deep Learning can achieve accurate computer-assisted diagnosis when large-scale annotated training samples are available. In Medical Imaging, unfortunately, preparing such massive annotated datasets is often unfeasible [6, 7]; to tackle this pervasive problem, researchers have proposed various data augmentation techniques, including Generative Adversarial Network (GAN)-based ones [8, 9, 10, 11, 12, 13] ; alternatively, Rauschecker *et al.* combined Convolutional Neural Networks (CNNs), feature engineering, and expert-knowledge Bayesian network to derive brain Magnetic Resonance Imaging (MRI) differential diagnoses that approach neuroradiologists' accuracy for 19 diseases. However, even exploiting these techniques, supervised learning still requires many images with pathological features, even for rare disease, to make a reliable diagnosis; nevertheless, it can only detect already-learned specific pathologies. In this regard, as physicians notice previously unseen anomaly examples using prior information on healthy body structure, unsupervised anomaly detection methods leveraging only large-scale healthy images can discover and alert overlooked diseases when their generalization fails.

Towards this, researchers reconstructed a single medical image *via* GANs [14], AutoEncoders (AEs) [15], or combining them, since GANs can generate realistic images and AEs, especially Variational AEs (VAEs), can directly map data onto its latent representation [16]; then, unseen images were scored by comparing them with reconstructed ones to discriminate a pathological image distribution (i.e., outliers either in the learned feature space or from high reconstruction loss). However, those single image reconstruction methods mainly target diseases easy-to-detect from a single image even for non-expert human observers, such as glioblastoma on MR images [16] and lung cancer on Computed Tomography (CT) images [15]. Without considering continuity between multiple adjacent images, they cannot directly discriminate diseases composed of the accumulation of subtle anatomical anomalies, such as AD. Moreover, no study has shown so far how unsupervised anomaly detection is associated with either disease stages, various (i.e., more than 2 types of) diseases, or multi-sequence MRI scans.

Therefore, this paper proposes unsupervised Medical Anomaly Detection GAN (MADGAN), a novel two-step method using GAN-based multiple adjacent brain MRI slice reconstruction to detect various diseases at various stages on multi-sequence structural MRI (Fig. 1): (*Reconstruction*) Wasserstein loss with Gradient Penalty (WGAN-GP) [17, 18] + 100 ℓ_1 loss—trained on 3 healthy brain axial MRI slices to reconstruct the next 3 ones—reconstructs unseen healthy/abnormal scans; the ℓ_1 loss generalizes well only for unseen images with a similar distribution to the training images while the WGAN-GP loss captures recognizable structure; (*Diagnosis*) Average ℓ_2 loss per scan discriminates them, comparing the ground truth/reconstructed slices; the ℓ_2 loss clearly discriminates the healthy/abnormal scans as squared error becomes huge for outliers. Using Receiver Operating Characteristics (ROCs) and their Area Under the Curves (AUCs), we evaluate the diagnosis performance of AD on T1-weighted (T1) MRI scans, and brain metastases/various

diseases (e.g., small infarctions, aneurysms) on contrast-enhanced T1 (T1c) MRI scans. Using $1,133$ healthy T1 and 135 healthy T1c scans for training, our Self-Attention (SA) MADGAN approach can detect AD at a very early stage, Mild Cognitive Impairment (MCI), with AUC 0.727, and AD at a late stage with AUC 0.894, while detecting brain metastases with AUC 0.921.

Contributions. Our main contributions are as follows:

- **MRI Slice Reconstruction:** This first multiple MRI slice reconstruction approach can reliably predict the next 3 slices from the previous 3 ones only for unseen images similar to training data by combining SAGAN and ℓ_1 loss.
- **Unsupervised Anomaly Detection:** This first unsupervised multi-stage anomaly detection reveals that, like physicians' way of performing a diagnosis, massive healthy data can aid early diagnosis, such as of MCI, while also detecting late-stage disease much more accurately by discriminating with ℓ_2 loss.
- **Various Disease Diagnosis:** This first unsupervised various disease diagnosis can reliably detect the accumulation of subtle anatomical anomalies (e.g., AD), as well as hyper-intense enhancing lesions (e.g., brain metastases) on multi-sequence MRI scans.

Related work

Alzheimer's disease diagnosis

Even though the clinical, social, and economic impact of early AD diagnosis is of paramount importance [19]—primarily associated with MCI detection [20]—it generally relies on subjective assessment by physicians (e.g., neurologists, geriatricians, and psychiatrists). The diagnosis typically considers two characteristics: (*i*) mesial temporal lobe atrophy (particularly hippocampus, entorhinal cortex, and perirhinal cortex) and (*ii*) temporo-parietal cortical atrophy. Quantifying these structures is crucial for early AD diagnosis and its progression tracking [21]. Moreover, morphometry-based markers, such as gray matter volume and cortical thickness, can play a key role in brain atrophy assessment [22].

Towards quantitative and reproducible approaches, many traditional supervised Machine Learning-based methods—which relies on handcrafted MRI-derived features—were proposed in the literature [23, 24]. In this context, diffusion-weighted MRI tractography enables reconstructing the brain's physical connections that can be subsequently investigated by complex network-based techniques. Lella *et al.* [25] employed the whole brain structural communicability as a graph-based metric to describe the AD-relevant brain connectivity disruption. This approach achieved comparable performance with classic Machine Learning models—namely, Support Vector Machines, Random Forests, and Artificial Neural Networks—in terms of classification and feature importance analysis.

In the latest years, Deep Learning has achieved outstanding performance by exploiting more multiple levels of abstraction and descriptive embeddings in a hierarchy of increasingly complex features [26]: Liu *et al.* devised a semi-supervised CNN to significantly reduce the need for labeled training data [27]; for clinical decision-making tasks, Suk *et al.* integrated multiple sparse regression models (i.e., Deep

Ensemble Sparse Regression Network) [28]; Spasov *et al.* proposed a parameter-efficient CNN for 3D separable convolutions, combining dual learning and a specific layer to predict the conversion from MCI to AD within 3 years [29]; different from CNN-based approaches, Parisot used a semi-supervised Graph Convolutional Network trained on a sub-set of labeled nodes with diagnostic outcomes to represent sparse clinical data [30]. However, to the best of our knowledge, no existing work has conducted fully unsupervised anomaly detection for AD diagnosis since capturing subtle anatomical differences between MCI and AD is challenging.

Brain metastasis and various disease diagnosis

Along with neuro-degenerative diseases, MRI can also play a definite role in abnormality diagnosis. Whereas advanced cancer screening, imaging, and therapeutics can improve oncological patients' survival and quality of life, brain metastases still remain major contributors of morbidity and mortality, especially for patients with lung cancer, breast cancer, or malignant melanoma [31]. To tackle this, previous computational methods have detected the brain metastases in either supervised [13, 32] or semi-automatic manner [33, 34].

Detecting other various diseases, such as cerebral aneurysms, hemorrhage, and infarctions, also remain challenging [35, 36]. Therefore, similar to the brain metastases, researchers have mostly relied on supervised methods, especially CNN-based detection [37, 38, 39]. Recently, unsupervised anomaly segmentation methods have been applied to brain MRI datasets for detecting multiple sclerosis lesions [40] and glioblastoma [41]. However, it is difficult to directly compare our approach with such existing unsupervised anomaly detection methods on 3D medical images since we perform a whole-brain diagnosis (i.e., classification), instead of segmentation.

Unsupervised medical anomaly detection

Unsupervised disease diagnosis is challenging because it requires estimating healthy anatomy's normative distributions only from healthy examples to detect outliers either in the learned feature space or from high reconstruction loss. The latest advances in Deep Learning, mostly GANs [8] and VAEs [42], have allowed for the accurate estimation of the high-dimensional healthy distributions. Except for discriminative-boundary-based approaches including [43], almost all unsupervised medical anomaly detection studies have leveraged reconstruction: as pioneering research, Schlegl *et al.* proposed AnoGAN to detect outliers in the learned feature space of the GAN [44]; then, the same authors presented fast AnoGAN that can efficiently map query images onto the latent space [14]; since the reconstruction-based models often suffer from many false positives, Chen *et al.* penalized large deviations between original/reconstructed images in gliomas and stroke lesion detection on brain MRI [45]. However, to the best of our knowledge, all previous studies are based on 2D/3D single image reconstruction, without considering continuity between multiple adjacent slices. Moreover, no existing work has investigated how unsupervised anomaly detection is associated with either disease stages, various (i.e., more than two types of) diseases, or multi-sequence MRI scans.

Self-Attention GANs (SAGANs)

Zhang *et al.* proposed SAGAN that deploys an SA mechanism in the generator/discriminator of a GAN to learn global and long-range dependencies for diverse image generation [46]; for further performance improvement, they suggested to apply the SA modules to large feature maps. The SAGANs have shown great promise in various tasks, such as human pose estimation [47], image colorization [48], photo-realistic image de-quantization [49], and large-scale image generation [50]. This SAGAN trend also applies to Medical Imaging to extract multi-level features for better super-resolution/denoising and lesion characterization: to mitigate the problem of thin slice thickness, Kudo *et al.* and Li *et al.* applied the SA modules to GANs on CT and MRI scans, respectively [51, 52]; similarly, in [53], the authors proposed to fuse plane SA modules and depth SA modules for low-dose 3D CT denoising; Lan *et al.* synthesized multi-modal 3D brain images using SA conditional GAN [53]; Ali *et al.* incorporated SA modules into progressive growing of GANs to generate realistic and diverse skin lesion images for data augmentation [54]. However, to the best of our knowledge, no existing work has directly exploited the SAGAN for medical disease diagnosis.

Materials and methods

Datasets

AD dataset: OASIS-3

We use a longitudinal 3.0T MRI dataset of $176 \times 240/176 \times 256$ T1 brain axial MRI slices containing both normal aging subjects/AD patients, extracted from the Open Access Series of Imaging Studies-3 (OASIS-3) [55]. The 176×240 slices are zero-padded to reach 176×256 pixels. Relying on Clinical Dementia Rating (CDR) [56], common clinical scale for the staging of dementia, the subjects are comprised of:

- Unchanged CDR $= 0$: Cognitively healthy population;
- CDR $= 0.5$: Very mild dementia ($\sim$ MCI);
- CDR $= 1$: Mild dementia;
- CDR $= 2$: Moderate dementia.

Since our dataset is longitudinal and the same subject's CDRs may vary (e.g., CDR $= 0$ to CDR $= 0.5$), we only use scans with unchanged CDR $= 0$ to assure certainly healthy scans. As CDRs are not always assessed simultaneously with the MRI acquisition, we label MRI scans with CDRs at the closest date. We only select brain MRI slices including hippocampus/amygdala/ventricles among whole 256 axial slices per scan to avoid over-fitting from AD-irrelevant information; the atrophy of the hippocampus/amygdala/cerebral cortex, and enlarged ventricles are strongly associated with AD, and thus they mainly affect the AD classification performance of Machine Learning [57]. Moreover, we discard low-quality MRI slices. The remaining dataset is divided as follows:

- Training set: Unchanged CDR $= 0$ (408 subjects/$1,133$ scans/$57,834$ slices);
- Test set: Unchanged CDR $= 0$ (168 subjects/473 scans/$24,278$ slices),
  CDR $= 0.5$ (152 subjects/253 scans/$13,813$ slices),
  CDR $= 1$ (90 subjects/135 scans/$7,532$ slices),
  CDR $= 2$ (6 subjects/10 scans/500 slices).

The same subject's scans are included in the same dataset. The datasets are strongly biased towards healthy scans similar to MRI inspection in the clinical routine. During training for reconstruction, we only use the training set—structural MRI alone—containing healthy slices to conduct unsupervised learning. We do not use a validation set as our unsupervised diagnosis step is non-trainable.

Brain metastasis and various disease dataset

This paper also uses a non-longitudinal, heterogeneous 1.5T/3.0T MRI dataset of $190 \times 224/216 \times 256/256 \times 256/460 \times 460$ T1c brain axial MRI slices. This dataset was collected by the authors at the National Center for Global Health and Medicine, Tokyo, Japan, and is currently not publicly available due to ethical restrictions. The dataset contains both healthy subjects, brain metastasis patients [33], and patients with various diseases different from brain metastases. The slices are resized to 176×256 pixels. The various diseases include but are not limited to:

- Small infarctions;
- Aneurysms;
- Benign tumors;
- Hemorrhages;
- Cysts;
- White matter lesions;
- Post-operative inflammations.

Conforming to T1 slices, we also only select T1c slices including hippocampus, amygdala, and ventricles—a large portion of various diseases also appear in the mid-brain. The remaining dataset is divided as follows:

- Training set: Normal (135 subjects/135 scans/$7,793$ slices);
- Test set: Normal (58 subjects/58 scans/$3,353$ slices),
  Brain Metastases (79 subjects/79 scans/$4,872$ slices),
  Various Diseases (66 subjects/66 scans/$4,195$ slices).

Since we cannot collect large-scale T1c scans from healthy patients like OASIS-3 dataset, during training for reconstruction, we use both T1/T1c training sets containing healthy slices simultaneously for the knowledge transfer. In the clinical practice, T1c MRI is well-established in detecting various diseases, including brain metastases [58], thanks to its high-contrast in the enhancing region—however, the contrast agent is not suitable for screening studies. Accordingly, such inter-sequence knowledge transfer is valuable in computer-assisted MRI diagnosis. During testing, we make an unsupervised diagnosis on T1 and T1c scans separately.

MADGAN-based multiple adjacent brain MRI slice reconstruction

To model strong consistency in healthy brain anatomy (Fig. 1), in each scan, we reconstruct the next 3 MRI slices from the previous 3 ones using an image-to-image GAN (e.g., if a scan includes 40 slices s_i for $i = 1, \ldots, 40$, we reconstruct all possible 35 setups: $(s_i)_{i \in \{1,2,3\}} \mapsto (s_i)_{i \in \{4,5,6\}}$; $(s_i)_{i \in \{2,3,4\}} \mapsto (s_i)_{i \in \{5,6,7\}}$; $\ldots$; $(s_i)_{i \in \{35,36,37\}} \mapsto (s_i)_{i \in \{38,39,40\}}$). As Fig. 2 shows, our MADGAN uses a U-Net-like [59, 60] generator with 4 convolutional layers in encoders and 4 deconvolutional layers in decoders respectively with skip connections, as well as a discriminator with 3 decoders. We apply batch normalization to both convolution with Leaky Rectified Linear Unit (ReLU) and deconvolution with ReLU. Between the designated

convolutional/deconvolutional layers and batch normalization layers, we apply SA modules [46] for effective knowledge transfer *via* feature recalibration between T1 and T1c slices; as confirmed on four different image datasets [61], introducing the SA modules to GAN-based anomaly detection (i.e., attention-driven, long-range dependency modeling) can also mitigate the effect of noise by ignoring irrelevant disturbances and focusing on the salient body parts in the slice. We compare the MADGAN models with a different number of the SA modules: (*i*) no SA modules (i.e., MADGAN); (*ii*) 3 (red-contoured) SA modules (i.e., 3-SA MADGAN); (*iii*) 7 (red- and blue-contoured) SA modules (i.e., 7-SA MADGAN). To confirm how reconstructed slices' realism and anatomical continuity affect medical anomaly detection, we also compare the MADGAN models with different loss functions: (*i*) WGAN-GP loss + 100 ℓ_1 loss (i.e., MADGAN); (*ii*) WGAN-GP loss (i.e., MADGAN w/o ℓ_1 loss). The ℓ_1 and ℓ_2 losses between an input image x and its reconstructed image x' are defined as follows:

$$\ell_1 = \sum_{i=1}^{P} |x_i - x'_i|, \tag{1}$$

$$\ell_2 = \sum_{i=1}^{P} (x - x')^2, \tag{2}$$

where P denotes the number of pixels.

Implementation details   Each MADGAN training lasts for 1.8×10^6 steps with a batch size of 16 (our maximum available batch size). We use 2.0×10^{-4} learning rate for Adam optimizer [62]. Such as in RGB images, we concatenate adjacent 3 grayscale slices into 3 channels. During training, the generator uses two dropout [63] layers with 0.5 rate. We flip the discriminator's real/synthetic labels once in three times for robustness. Using 4 NVIDIA Quadro GV100 graphics processing units, we implement the framework on TensorFlow 1.8.

Unsupervised medical anomaly detection

During diagnosis, we classify unseen healthy and abnormal scans based on average ℓ_2 loss per scan. The average ℓ_2 loss is calculated from whole MADGAN-reconstructed 3 slices s_i of each scan containing n slices: $(s_i)_{i \in \{4,5,6\}}$; $(s_i)_{i \in \{5,6,7\}}$; $\ldots$; $(s_i)_{i \in \{n-2,n-1,n\}}$. We use the ℓ_2 loss since squared error is sensitive to outliers and it significantly outperformed other losses (i.e., ℓ_1 loss, Dice loss, Structural Similarity loss) in our preliminary paper [64]. To evaluate its unsupervised AD diagnosis performance on a T1 MRI test set, we show ROCs—along with the AUC values—between CDR = 0 *vs* (*i*) all the other CDRs; (*ii*) CDR = 0.5; (*iii*) CDR = 1; (*iv*) CDR = 2. We also show the AUCs under different training steps (i.e., 150k, 300k, 600k, 900k, 1.8M steps) and confirm the effect of calculating average ℓ_2 loss (among whole slice sets or continuous 10 slice sets exhibiting the highest loss) per scan; if the 10 slice sets start from the j-th slice, we use: $(s_i)_{i \in \{j,j+1,j+2\}}$; $(s_i)_{i \in \{j+1,j+2,j+3\}}$; $\ldots$; $(s_i)_{i \in \{j+9,j+10,j+11\}}$). Moreover, we visualize pixelwise ℓ_2 loss between real/reconstructed 3 slices, along with distributions of average ℓ_2 loss per scan of CDR = 0/0.5/1/2 to know how disease stages affect its discrimination.

In exactly the same manner, we evaluate the diagnosis performance of brain metastases/various diseases on a T1c MRI test set, showing ROCs/AUCs between normal *vs* (*i*) brain metastases + various diseases; (*ii*) brain metastases; (*iii*) various diseases.

Results

Reconstructed brain MRI slices

Fig. 3 illustrates example real T1 MRI slices from a test set and their reconstruction by MADGAN and 7-SA MADGAN. Similarly, Figs. 4 and 5 show example real T1c MRI slices and their reconstructions. Pixelwise ℓ_2 loss tends to increase (i.e., high intensity in the heatmap) around lesions due to their different image distribution from healthy samples.

Figs. 6 and 7 indicate distributions of average ℓ_2 loss per scan on T1 and T1c scans, respectively. Leveraging ℓ_1 loss' good realism sacrificing diversity (i.e., generalizing well only for unseen images with a similar distribution to training images) and WGAN-GP loss' ability to capture recognizable structure, the MADGAN can successfully capture T1-specific appearance and anatomical changes from the previous 3 slices. Meanwhile, the 7-SA MADGAN tends to be less stable in keeping texture but more sensitive to abnormal anatomical changes due to the SA modules' anomaly-sensitive reconstruction *via* the attention-driven, long-range dependency modeling, resulting in moderately higher average ℓ_2 loss than the MADGAN.

Since the models are trained only on healthy slices, as visualized by an overimposed Jet colormap, reconstructing slices with higher CDRs tends to comparatively fail, especially around hippocampus, amygdala, cerebral cortex, and ventricles due to their insufficient atrophy after reconstruction; this is plausible because physicians also perform the AD diagnosis based on their prior normal atrophy information around those body parts. We do not find other significant reconstruction failures except them, considering that inter-subject/sequence variability also lead to considerable reconstruction failures. The T1c scans show much lower average ℓ_2 loss than the T1 scans due to darker texture. Since most training images are the T1 slices with brighter texture than the T1c slices, reconstruction quality clearly decreases on the T1c slices, occasionally exhibiting bright texture. Accordingly, reconstruction failure from anomaly contributes comparatively less to the average ℓ_2 loss, especially when local small lesions, such as brain abscess and enhanced lesions, appear—unlike global big lesions, such as multiple cerebral infarction and blood component retention. However, the average ℓ_2 loss remarkably increases on brain metastases scans due to their hyper-intensity, especially for the 7-SA MADGAN.

Unsupervised anomaly detection results

Figs. 8 and 9 show AUCs of unsupervised anomaly detection on T1 and T1c scans under different training steps, respectively. The AUCs generally increase as training progresses, but more SA modules require more training steps until convergence due to their feature recalibration. Although most models show a convergence after 900k steps, MADGAN with abundant SA modules might perform even better, especially on the T1c scans with less training data than the T1 scans, if we continue its training.

All the best results in specific tasks, except for CDR $= 0$ *vs* CDR $= 0.5$, are from the SA models (e.g., 7-SA MADGAN w/o ℓ_1 loss under 900k steps: AUC 0.783 in CDR $= 0$ *vs* CDR $= 0.5 + 1 + 2$, 3-SA MADGAN under 300k steps: AUC 0.966 in normal *vs* brain metastases, 3-SA MADGAN under 600k steps: AUC 0.638 in normal *vs* various diseases); thus, whereas the SA models, which do not know the task to optimize in an unsupervised manner, perform unstably, we might use them similarly to supervised learning if we could obtain good parameters for a certain disease. Without ℓ_1 loss, the AUCs tend to decrease, also accompanying large fluctuations; 7-SA MADGAN w/o ℓ_1 loss performs well on the T1 scans but poorly on the T1c scans due to the instability.

Figs. 10 and 11 illustrate ROC curves and their AUCs on T1 and T1c scans under 1.8M training steps, respectively. Since brains with higher CDRs accompany stronger anatomical atrophy from healthy brains, their AUCs between unchanged CDR $= 0$ remarkably increase as CDRs increase. MADGAN and 7-SA MADGAN both achieves good AUCs, especially for higher CDRs—The MADGAN obtains AUC 0.750/0.707/0.829 in CDR $= 0$ *vs* CDR $= 0.5/1/2$, respectively; the discrimination between healthy subjects *vs* MCI patients (i.e., CDR $= 0$ *vs* CDR $= 0.5$) is extremely difficult even in a supervised manner [57]. Whereas detecting various diseases is difficult in an unsupervised manner, the 7-SA MADGAN outperforms the MADGAN and achieves AUC 0.921 in brain metastases detection. As Tables 1 and 2 show, the effect of how to calculate average ℓ_2 loss (among whole slice sets or continuous 10 slice sets exhibiting the highest loss) per scan is limited. Whereas no significant differences exist between them, the best performing approach on each dataset is always whole slice sets-based.

Discussion and conclusions

Using massive healthy data, our MADGAN-based multiple MRI slice reconstruction can reliably discriminate AD patients from healthy subjects for the first time in an unsupervised manner; to detect the accumulation of subtle anatomical anomalies, our solution leverages a two-step approach: (*Reconstruction*) ℓ_1 loss generalizes well only for unseen images with a similar distribution to training images while WGAN-GP loss captures recognizable structure; (*Diagnosis*) ℓ_2 loss clearly discriminates healthy/abnormal data as squared error becomes huge for outliers. Using $1,133$ healthy T1 MRI scans for training, our approach can detect AD at a very early stage, MCI, with AUC 0.727 while detecting AD at a late stage with AUC 0.894. Accordingly, this first unsupervised anomaly detection across different disease stages reveals that, like physicians' way of performing a diagnosis, large-scale healthy data can reliably aid early diagnosis, such as of MCI, while also detecting late-stage disease much more accurately.

To confirm its ability to also detect other various diseases, even on different MRI sequence scans, we firstly investigate how unsupervised medical anomaly detection is associated with various diseases and multi-sequence MRI scans, respectively. Due to the different texture of T1/T1c slices, reconstruction quality clearly decreases on the data-sparse T1c slices, and thus reconstruction failure from anomaly contributes comparatively less to the average ℓ_2 loss. Nevertheless, we generally succeed to unravel diseases hard-to-detect and easy-to-detect in an unsupervised manner: it

is hard to detect local small lesions, such as brain abscess and enhanced lesions; but, it is easy to detect hyper-intense enhancing lesions, such as brain metastases (AUC 0.921), especially for 7-SA MADGAN thanks to its feature recalibration. Our visualization of differences between real/reconstructed slices might play a key role in understanding and preventing various diseases, including rare disease.

Since we firstly propose a two-step unsupervised anomaly detection approach based on multiple slice reconstruction, its limitations are two-fold: yet less generalizable reconstruction and diagnosis. As future work, we will investigate more suitable SA modules in a reconstruction model, such as Dual Attention Network that capture feature dependencies in both spatial/channel dimensions [65]; here, optimizing where to place how many SA modules is the most relevant aspect. We will validate combining new loss functions for both reconstruction/diagnosis, including sparsity regularization [66], structural similarity [67], and perceptual loss [68]. Lastly, we plan to collect a higher amount of healthy T1c scans to reliably detect and locate various diseases, including cancers and rare diseases. Integrating multi-modal imaging data, such as Positron Emission Tomography with specific radiotracers [69], might further improve disease diagnosis [70], even when analyzed modalities are not always available [71]. Moreover, to specify detected anomalies, we might extend this work to supervised learning with limited pathological data by discriminating normal/pathological image distributions during diagnosis, instead of calculating the average ℓ_2 loss per scan.

List of abbreviations used
Area Under the Curve: AUCs, AutoEncoder: AE, Alzheimer's Disease: AD, Clinical Dementia Rating: CDR, Contrast-enhanced T1-weighted: T1c, Convolutional Neural Network: CNN, Computed Tomography: CT, Generative Adversarial Network: GAN, Magnetic Resonance Imaging: MRI, Medical Anomaly Detection Generative Adversarial Network: MADGAN, Mild Cognitive Impairment: MCI, Open Access Series of Imaging Studies-3: OASIS-3, Receiver Operating Characteristic: ROC, Rectified Linear Unit: ReLU, Self-Attention: SA, T1-weighted: T1, Variational AutoEncoder: VAE, Wasserstein loss with Gradient Penalty: WGAN-GP.

Competing interests
The authors declare that they have no competing interests.

Author's contributions
Conceived the idea: CH, LR, ZAM, KM. Designed the code: CH, LR, ZAM. Collected the T1c dataset: TN. Implemented the code: CH. Performed the experiments: CH. Analyzed the results: CH, LR. Wrote the manuscript: CH, LR. Critically read the manuscript and contributed to the discussion of the whole work: KM, TN, ZAM, YS, SK, ES, HN, SS.

Author details
[1]LPIXEL Inc., Tokyo, Japan. [2]Department of Radiology, University of Cambridge, Cambridge, United Kingdom. [3]Cancer Research UK Cambridge Centre, University of Cambridge, Cambridge, United Kingdom. [4]Research Center for Medical Big Data, National Institute of Informatics, Tokyo, Japan. [5]National Center for Global Health and Medicine, Tokyo, Japan. [6]Department of Radiology, Juntendo University, Tokyo, Japan. [7]Department of Artificial Intelligence, ELTE Eötvös Loránd University, Budapest, Hungary. [8]Graduate School of Information Science and Technology, The University of Tokyo, Tokyo, Japan. [9]International Research Center for Neurointelligence (WPI-IRCN), The University of Tokyo Institutes for Advanced Study, The University of Tokyo, Tokyo, Japan.
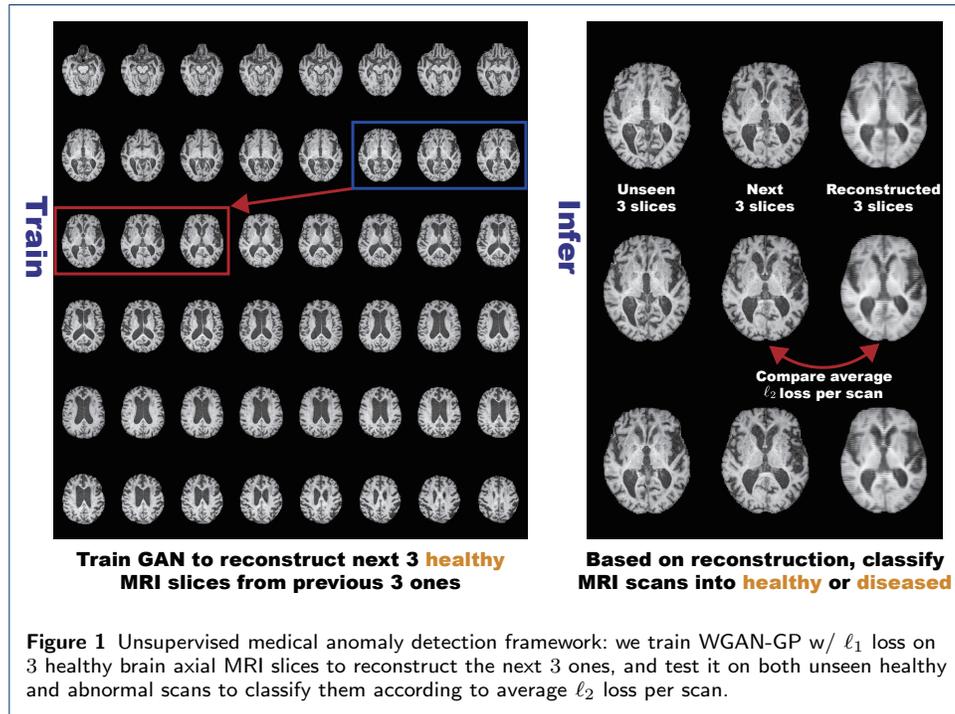
References
1. Gao, L., Pan, H., Li, Q., Xie, X., Zhang, Z., Han, J., Zhai, X.: Brain medical image diagnosis based on corners with importance-values. BMC Bionform **18**(1), 1–13 (2017). doi:10.1186/s12859-017-1903-6
2. Serra, A., Galdi, P., Tagliaferri, R.: Machine learning for bioinformatics and neuroimaging. Wiley Interdisc Rev Data Min Knowl Discov **8**(5), 1248 (2018). doi:10.1002/widm.1248

3. Park, B., Lee, W., Han, K.: Modeling the interactions of Alzheimer-related genes from the whole brain microarray data and diffusion tensor images of human brain **13**(S7), 10 (2012). doi:10.1186/1471-2105-13-S7-S10. Springer

4. Medland, S.E., Jahanshad, N., Neale, B.M., Thompson, P.M.: Whole-genome analyses of whole-brain data: working within an expanded search space. Nat Neurosci **17**(6), 791–800 (2014). doi:10.1038/nn.3718

5. Zhao, T., Hu, Y., Zang, T., Cheng, L.: Identifying Alzheimer's disease-related proteins by LRRGD. BMC Bionform **20**(18), 570 (2019). doi:10.1186/s12859-019-3124-7

6. Han, C., Rundo, L., Murao, K., Nemoto, T., Nakayama, H., Satoh, S.: Bridging the gap between AI and healthcare sides: towards developing clinically relevant AI-powered diagnosis systems. In: Proc. International Conference on Artificial Intelligence Applications and Innovations (AIAI), pp. 320–333 (2020). doi:10.1007/978-3-030-49186-4_27

7. Cheplygina, V., de Bruijne, M., Pluim, J.P.: Not-so-supervised: a survey of semi-supervised, multi-instance, and transfer learning in medical image analysis. Med Image Anal **54**, 280–296 (2019). doi:10.1016/j.media.2019.03.009

8. Goodfellow, I., Pouget-Abadie, J., Mirza, M., Xu, B., Warde-Farley, D., Ozair, S., *et al.*: Generative adversarial nets. In: Proc. Advances in Neural Information Processing Systems (NIPS), pp. 2672–2680 (2014)

9. Frid-Adar, M., Diamant, I., Klang, E., Amitai, M., Goldberger, J., Greenspan, H.: GAN-based synthetic medical image augmentation for increased CNN performance in liver lesion classification. Neurocomputing **321**, 321–331 (2018). doi:10.1016/j.neucom.2018.09.013

10. Han, C., Rundo, L., Araki, R., Furukawa, Y., Mauri, G., Nakayama, H., Hayashi, H.: Infinite brain MR images: PGGAN-based data augmentation for tumor detection. In: Neural Approaches to Dynamics of Signal Exchanges. Smart Innovation, Systems and Technologies, vol. 151, pp. 291–303. Springer, ??? (2019). doi:10.1007/978-981-13-8950-4_27

11. Han, C., Rundo, L., Araki, R., Nagano, Y., Furukawa, Y., *et al.*: Combining noise-to-image and image-to-image GANs: brain MR image augmentation for tumor detection. IEEE Access **7**(1), 156966–156977 (2019). doi:10.1109/ACCESS.2019.2947606

12. Han, C., Kitamura, Y., Kudo, A., Ichinose, A., Rundo, L., Furukawa, Y., *et al.*: Synthesizing diverse lung nodules wherever massively: 3D multi-conditional GAN-based CT image augmentation for object detection. In: Proc. International Conference on 3D Vision (3DV), pp. 729–737 (2019). doi:10.1109/3DV.2019.00085

13. Han, C., Murao, K., Noguchi, T., *et al.*: Learning more with less: Conditional PGGAN-based data augmentation for brain metastases detection using highly-rough annotation on MR images. In: Proc. ACM International Conference on Information and Knowledge Management (CIKM), pp. 119–127 (2019). doi:10.1145/3357384.3357890

14. Schlegl, T., Seeböck, P., Waldstein, S.M., Langs, G., Schmidt-Erfurth, U.: f-AnoGAN: fast unsupervised anomaly detection with generative adversarial networks. Med Image Anal **54**, 30–44 (2019)

15. Uzunova, H., Schultz, S., Handels, H., Ehrhardt, J.: Unsupervised pathology detection in medical images using conditional variational autoencoders. Int J Comput Assist Radiol Surg **14**(3), 451–461 (2019). doi:10.1007/s11548-018-1898-0

16. Chen, X., Konukoglu, E.: Unsupervised detection of lesions in brain MRI using constrained adversarial auto-encoders. In: Proc. International Conference on Medical Imaging with Deep Learning (MIDL) (2018). arXiv preprint arXiv:1806.04972

17. Gulrajani, I., Ahmed, F., Arjovsky, M., Dumoulin, V., Courville, A.C.: Improved training of Wasserstein GANs. In: Proc. Advances in Neural Information Processing Systems (NIPS), pp. 5769–5779 (2017)

18. Han, C., Hayashi, H., Rundo, L., Araki, R., Shimoda, W., Muramatsu, S., *et al.*: GAN-based synthetic brain MR image generation. In: Proc. International Symposium on Biomedical Imaging (ISBI), pp. 734–738 (2018). doi:10.1109/ISBI.2018.8363678. IEEE

19. Arvanitakis, Z., Shah, R.C., Bennett, D.A.: Diagnosis and management of dementia. JAMA **322**(16), 1589–1599 (2019). doi:10.1001/jama.2019.4782

20. Moscoso Rial, A., Silva Rodríguez, J., Aldrey Vázquez, J.M., Cortés Hernández, J., Fernández Ferreiro, A., Gómez Lado, N., *et al.*: Prediction of alzheimer's disease dementia with mri beyond the short-term: Implications for the design of predictive models. NeuroImage Clinical **23**, 101837 (2019). doi:10.1016/j.nicl.2019.101837

21. Desikan, R.S., Cabral, H.J., Fischl, B., Guttmann, C.R., Blacker, D., Hyman, B.T., *et al.*: Temporoparietal MR imaging measures of atrophy in subjects with mild cognitive impairment that predict subsequent diagnosis of Alzheimer disease. Am J Neuroradiol **30**(3), 532–538 (2009). doi:10.3174/ajnr.A1397

22. Ma, X., Li, Z., Jing, B., Liu, H., Li, D., Li, H.: Identify the atrophy of Alzheimer's disease, mild cognitive impairment and normal aging using morphometric MRI analysis. Front Aging Neurosci **8**, 243 (2016). doi:10.3389/fnagi.2016.00243

23. Salvatore, C., Cerasa, A., Battista, P., Gilardi, M.C., Quattrone, A., Castiglioni, I.: Magnetic resonance imaging biomarkers for the early diagnosis of Alzheimer's disease: a machine learning approach. Front Neurosci **9**, 307 (2015). doi:10.3389/fnins.2015.00307

24. Nanni, L., Brahnam, S., Salvatore, C., Castiglioni, I.: Texture descriptors and voxels for the early diagnosis of Alzheimer's disease. Artif. Intell. Med. **97**, 19–26 (2019). doi:10.1016/j.artmed.2019.05.003

25. Lella, E., Lombardi, A., Amoroso, N., Diacono, D., Maggipinto, T., Monaco, A., Bellotti, R., Tangaro, S.: Machine learning and DWI brain communicability networks for Alzheimer's disease detection. Appl Sci **10**(3), 934 (2020). doi:10.3390/app10030934

26. LeCun, Y., Bengio, Y., Hinton, G.: Deep learning. Nature **521**(7553), 436 (2015). doi:10.1038/nature145

27. Liu, S., Liu, S., Cai, W., Pujol, S., Kikinis, R., Feng, D.: Early diagnosis of alzheimer's disease with deep learning. In: Proc. International Symposium on Biomedical Imaging (ISBI), pp. 1015–1018 (2014). doi:10.1109/ISBI.2014.6868045. IEEE

28. Suk, H.-I., Lee, S.-W., Shen, D.: Deep ensemble learning of sparse regression models for brain disease diagnosis. Med. Image Anal. **37**, 101–113 (2017). doi:10.1016/j.media.2017.01.008

29. Spasov, S., Passamonti, L., Duggento, A., Liò, P., Toschi, N., Initiative, A.D.N., *et al.*: A parameter-efficient

deep learning approach to predict conversion from mild cognitive impairment to Alzheimer's disease. NeuroImage **189**, 276–287 (2019). doi:10.1016/j.neuroimage.2019.01.031

30. Parisot, S., Ktena, S.I., Ferrante, E., Lee, M., Guerrero, R., Glocker, B., Rueckert, D.: Disease prediction using graph convolutional networks: application to autism spectrum disorder and Alzheimer's disease. Med Image Anal **48**, 117–130 (2018). doi:10.1016/j.media.2018.06.001

31. Sacks, P., Rahman, M.: Epidemiology of brain metastases. Neurosurg Clin **31**(4), 481–488 (2020). doi:10.1016/j.nec.2020.06.001

32. Grøvik, E., Yi, D., Iv, M., Tong, E., Rubin, D., Zaharchuk, G.: Deep learning enables automatic detection and segmentation of brain metastases on multisequence MRI. J Magn Reson Imaging **51**(1), 175–182 (2020). doi:10.1002/jmri.26766

33. Rundo, L., Militello, C., Russo, G., Vitabile, S., Gilardi, M.C., Mauri, G.: GTVcut for neuro-radiosurgery treatment planning: an MRI brain cancer seeded image segmentation method based on a cellular automata model. Nat Comput **17**, 521–536 (2018). doi:10.1007/s11047-017-9636-z

34. Rundo, L., Militello, C., Tangherloni, A., Russo, G., Vitabile, S., Gilardi, M.C., Mauri, G.: NeXt for neuro-radiosurgery: a fully automatic approach for necrosis extraction in brain tumor MRI using an unsupervised machine learning technique. Int J Imaging Syst Technol **28**(1), 21–37 (2018). doi:10.1002/ima.22253

35. Miki, S., Hayashi, N., Masutani, Y., Nomura, Y., Yoshikawa, T., Hanaoka, S., Nemoto, M., Ohtomo, K.: Computer-assisted detection of cerebral aneurysms in MR angiography in a routine image-reading environment: effects on diagnosis by radiologists. Am J Neuroradiol **37**(6), 1038–1043 (2016). doi:10.3174/ajnr.A4671

36. Vert, C., Parra-Fariñas, C., Rovira, À.: MR imaging in hyperacute ischemic stroke. Eur J Radiol **96**, 125–132 (2017). doi:10.1016/j.ejrad.2017.06.013

37. Zhou, M., Wang, X., Wu, Z., Pozo, J.M., Frangi, A.F.: Intracranial aneurysm detection from 3D vascular mesh models with ensemble deep learning. In: Proc. International Conference on Medical Image Computing and Computer-Assisted Intervention (MICCAI). LNCS, vol. 11767, pp. 243–252 (2019). doi:10.1007/978-3-030-32251-9_27. Springer

38. Conti, V., Militello, C., Rundo, L., Vitabile, S.: A novel bio-inspired approach for high-performance management in service-oriented networks. IEEE Trans Emerg Topics Comput (2020). doi:10.1109/TETC.2020.3018312. In press

39. Federau, C., Christensen, S., Scherrer, N., Ospel, J.M., Schulze-Zachau, V., Schmidt, N., *et al.*: Improved segmentation and detection sensitivity of diffusion-weighted stroke lesions with synthetically enhanced deep learning. Radiol Artif Intell **2**(5), 190217 (2020). doi:10.1148/ryai.2020190217

40. Baur, C., Wiestler, B., Albarqouni, S., Navab, N.: Deep autoencoding models for unsupervised anomaly segmentation in brain mr images. In: Proc. International Conference on Medical Image Computing and Computer-Assisted Intervention (MICCAI) Workshop, pp. 161–169 (2018). Springer

41. Zimmerer, D., Isensee, F., Petersen, J., Kohl, S., Maier-Hein, K.: Unsupervised anomaly localization using variational auto-encoders. In: Proc. International Conference on Medical Image Computing and Computer-Assisted Intervention (MICCAI), pp. 289–297 (2019). Springer

42. Kingma, D.P., Welling, M.: Auto-encoding variational Bayes. In: Proc. International Conference on Learning Representations (ICLR) (2014). arXiv preprint arXiv:1312.6114

43. Alaverdyan, Z., Jung, J., Bouet, R., Lartizien, C.: Regularized siamese neural network for unsupervised outlier detection on brain multiparametric magnetic resonance imaging: application to epilepsy lesion screening. Med Image Anal **60**, 101618 (2020)

44. Schlegl, T., Seeböck, P., Waldstein, S.M., Schmidt-Erfurth, U., Langs, G.: Unsupervised anomaly detection with generative adversarial networks to guide marker discovery. In: Proc. International Conference on Medical Image Computing and Computer-Assisted Intervention (MICCAI), pp. 146–157 (2017). Springer

45. Chen, X., You, S., Tezcan, K.C., Konukoglu, E.: Unsupervised lesion detection via image restoration with a normative prior. Med Image Anal, 101713 (2020). doi:10.1016/j.media.2020.101713

46. Zhang, H., Goodfellow, I., Metaxas, D., Odena, A.: Self-attention generative adversarial networks. In: Proc. International Conference on Machine Learning (ICML). PMLR, vol. 97, pp. 7354–7363 (2019). arXiv preprint arXiv:1805.08318

47. Wang, X., Cao, Z., Wang, R., Liu, Z., Zhu, X.: Improving human pose estimation with self-attention generative adversarial networks. IEEE Access **7**, 119668–119680 (2019). doi:10.1109/ACCESS.2019.2936709

48. Sharma, M., Makwana, M., Upadhyay, A., Singh, A.P., Badhwar, A., Trivedi, A., Saini, A., Chaudhury, S.: Robust image colorization using self attention based progressive generative adversarial network. In: Proc. IEEE/CVF Conference on Computer Vision and Pattern Recognition Workshops (CVPRW), pp. 2188–2196 (2019). doi:10.1109/CVPRW.2019.00272. IEEE

49. Zhang, Y., Hu, C., Lu, X.: Deep attentive generative adversarial network for photo-realistic image de-quantization. arXiv preprint arXiv:2004.03150 (2020)

50. Brock, A., Donahue, J., Simonyan, K.: Large scale GAN training for high fidelity natural image synthesis. In: Proc. International Conference on Learning Representations (ICLR) (2018). arXiv preprint arXiv:1809.11096

51. Kudo, A., Kitamura, Y., Li, Y., Iizuka, S., Simo-Serra, E.: Virtual thin slice: 3D conditional GAN-based super-resolution for CT slice interval. In: Proc. International Conference on Medical Image Computing and Computer-Assisted Intervention (MICCAI) Workshop. LNCS, vol. 11905, pp. 91–100 (2019). doi:10.1007/978-3-030-33843-5_9. Springer

52. Li, Y., Huang, H., Zhang, L., Wang, G., Zhang, H., Zhou, W.: Super-resolution and self-attention with generative adversarial network for improving malignancy characterization of hepatocellular carcinoma. In: Proc. IEEE 17th International Symposium on Biomedical Imaging (ISBI), pp. 1556–1560 (2020). doi:10.1109/ISBI45749.2020.9098705. IEEE

53. Lan, H., Toga, A.W., Sepehrband, F., Initiative, A.D.N., *et al.*: SC-GAN: 3D self-attention conditional GAN with spectral normalization for multi-modal neuroimaging synthesis. bioRxiv (2020). doi:10.1101/2020.06.09.143297

54. Ali, I.S., Mohamed, M.F., Mahdy, Y.B.: Data augmentation for skin lesion using self-attention based

progressive generative adversarial network. arXiv preprint arXiv:1910.11960 (2019)

55. LaMontagne, P.J., Keefe, S., Lauren, W., *et al.*: OASIS-3: longitudinal neuroimaging, clinical, and cognitive dataset for normal aging and Alzheimer's disease. Alzheimers Dement **14**(7), 1097 (2018). doi:10.1016/j.jalz.2018.06.1439

56. Morris, J.C.: The Clinical Dementia Rating (CDR): current version and scoring rules. Neurology **43**(11), 2412–2414 (1993). doi:10.1212/wnl.43.11.2412-a

57. Ledig, C., Schuh, A., Guerrero, R., Heckemann, R.A., Rueckert, D.: Structural brain imaging in Alzheimer's disease and mild cognitive impairment: biomarker analysis and shared morphometry database. Sci Rep **8**, 11258 (2018). doi:10.1038/s41598-018-29295-9

58. Arvold, N.D., Lee, E.Q., Mehta, M.P., Margolin, K., Alexander, B.M., *et al.*: Updates in the management of brain metastases. Neuro Oncol **18**(8), 1043–1065 (2016). doi:10.1093/neuonc/now127

59. Ronneberger, O., Fischer, P., Brox, T.: U-Net: Convolutional networks for biomedical image segmentation. In: Proc. International Conference on Medical Image Computing and Computer-Assisted Intervention (MICCAI). LNCS, vol. 9351, pp. 234–241. Springer, ??? (2015). doi:10.1007/978-3-319-24574-4_28

60. Rundo, L., Han, C., Nagano, Y., *et al.*: USE-Net: incorporating squeeze-and-excitation blocks into U-Net for prostate zonal segmentation of multi-institutional MRI datasets. Neurocomputing **365**, 31–43 (2019). doi:10.1016/j.neucom.2019.07.006

61. Kimura, D., Chaudhury, S., Narita, M., Munawar, A., Tachibana, R.: Adversarial discriminative attention for robust anomaly detection. In: Proc. IEEE Winter Conference on Applications of Computer Vision (WACV), pp. 2172–2181 (2020). doi:10.1109/WACV45572.2020.9093428

62. Kingma, D.P., Ba, J.: Adam: A method for stochastic optimization. arXiv preprint arXiv:1412.6980 (2014)

63. Srivastava, N., Hinton, G., Krizhevsky, A., Sutskever, I., Salakhutdinov, R.: Dropout: a simple way to prevent neural networks from overfitting. JMLR **15**(1), 1929–1958 (2014)

64. Han, C., Rundo, L., Murao, K., Milacski, Z.Á., Umemoto, K., Sala, E., Nakayama, H., Satoh, S.: GAN-based multiple adjacent brain MRI slice reconstruction for unsupervised Alzheimer's disease diagnosis. In: Proc. International Conference on Computational Intelligence Methods for Bioinformatics and Biostatistics (CIBB). LNBI (2020). arXiv preprint arXiv:1906.06114

65. Fu, J., Liu, J., Tian, H., Li, Y., Bao, Y., Fang, Z., Lu, H.: Dual attention network for scene segmentation. In: Proc. IEEE/CVF Conference on Computer Vision and Pattern Recognition (CVPR), pp. 3146–3154 (2019). doi:10.1109/CVPR.2019.00326. IEEE

66. Zhou, K., Gao, S., Cheng, J., Gu, Z., Fu, H., Tu, Z., Yang, J., Zhao, Y., Liu, J.: Sparse-GAN: sparsity-constrained generative adversarial network for anomaly detection in retinal OCT image. In: Proc. IEEE International Symposium on Biomedical Imaging (ISBI), pp. 1227–1231 (2020). doi:10.1109/ISBI45749.2020.9098374. IEEE

67. Haselmann, M., Gruber, D.P., Tabatabai, P.: Anomaly detection using deep learning based image completion. In: Proc. IEEE International Conference on Machine Learning and Applications (ICMLA), pp. 1237–1242 (2018). doi:10.1109/ICMLA.2018.00201. IEEE

68. Tuluptceva, N., Bakker, B., Fedulova, I., Schulz, H., Dylov, D.V.: Anomaly detection with deep perceptual autoencoders. arXiv preprint arXiv:2006.13265 (2020)

69. Rundo, L., Stefano, A., Militello, C., Russo, G., Sabini, M.G., D'Arrigo, C., Marletta, F., Ippolito, M., Mauri, G., Vitabile, S., Gilardi, M.C.: A fully automatic approach for multimodal PET and MR image segmentation in Gamma Knife treatment planning. Comput Methods Programs Biomed **144**, 77–96 (2017). doi:10.1016/j.cmpb.2017.03.011

70. Brier, M.R., Gordon, B., Friedrichsen, K., McCarthy, J., Stern, A., Christensen, J., Owen, C., Aldea, P., Su, Y., Hassenstab, J., *et al.*: Tau and Aβ imaging, CSF measures, and cognition in Alzheimer's disease. Sci Trans Med **8**(338), 338–6633866 (2016). doi:10.1126/scitranslmed.aaf2362

71. Li, R., Zhang, W., Suk, H.-I., Wang, L., Li, J., Shen, D., Ji, S.: Deep learning based imaging data completion for improved brain disease diagnosis. In: Proc. International Conference on Medical Image Computing and Computer-Assisted Intervention (MICCAI). LNCS, vol. 8675, pp. 305–312 (2014). doi:10.1007/978-3-319-10443-0_39. Springer

Figures

Train GAN to reconstruct next 3 healthy MRI slices from previous 3 ones

Based on reconstruction, classify MRI scans into healthy or diseased

Figure 1 Unsupervised medical anomaly detection framework: we train WGAN-GP w/ ℓ_1 loss on 3 healthy brain axial MRI slices to reconstruct the next 3 ones, and test it on both unseen healthy and abnormal scans to classify them according to average ℓ_2 loss per scan.

Figure 2 Proposed MADGAN architecture for the next 3-slice generation from the input 3 256×176 brain MRI slices: 3-SA MADGAN has only 3 (red-contoured) SA modules after convolution/deconvolution whereas 7-SA MADGAN has 7 (red- and blue-contoured) SA modules. Similar to RGB images, we concatenate adjacent 3 gray slices into 3 channels.
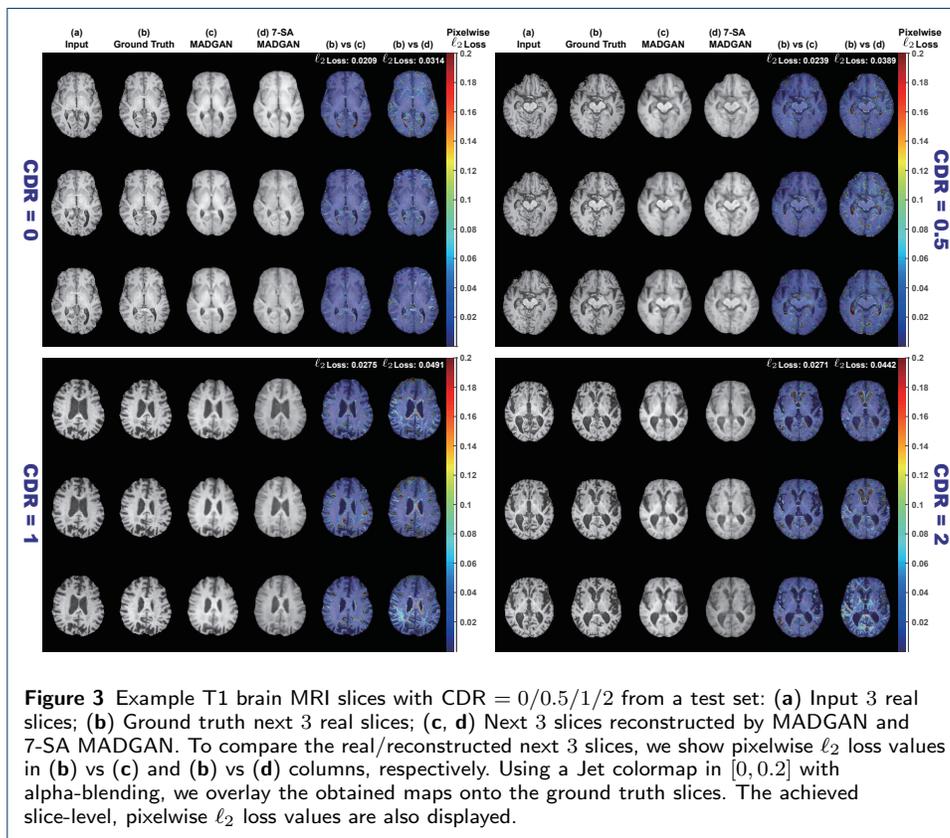
Figure 3 Example T1 brain MRI slices with CDR $= 0/0.5/1/2$ from a test set: (**a**) Input 3 real slices; (**b**) Ground truth next 3 real slices; (**c, d**) Next 3 slices reconstructed by MADGAN and 7-SA MADGAN. To compare the real/reconstructed next 3 slices, we show pixelwise ℓ_2 loss values in (**b**) vs (**c**) and (**b**) vs (**d**) columns, respectively. Using a Jet colormap in $[0, 0.2]$ with alpha-blending, we overlay the obtained maps onto the ground truth slices. The achieved slice-level, pixelwise ℓ_2 loss values are also displayed.

Figure 4 Example T1c brain MRI slices with no abnormal findings/three brain metastases from a test set: (**a**) Input 3 real slices; (**b**) Ground truth next 3 real slices; (**c**, **d**) Next 3 slices reconstructed by MADGAN and 7-SA MADGAN. To compare the real/reconstructed next 3 slices, we show pixelwise ℓ_2 loss values in (**b**) vs (**c**) and (**b**) vs (**d**) columns, respectively. Using a Jet colormap in $[0, 0.06]$ with alpha-blending, we overlay the obtained maps onto the ground truth slices. The achieved slice-level, pixelwise ℓ_2 loss values are also displayed.

Figure 5 Example T1c brain MRI slices with four different brain diseases from a test set: (**a**) Input 3 real slices; (**b**) Ground truth next 3 real slices; (**c**, **d**) Next 3 slices reconstructed by MADGAN and 7-SA MADGAN. To compare the real/reconstructed next 3 slices, we show pixelwise ℓ_2 loss values in (**b**) vs (**c**) and (**b**) vs (**d**) columns, respectively. Using a Jet colormap in $[0, 0.06]$ with alpha-blending, we overlay the obtained maps onto the ground truth slices. The achieved slice-level, pixelwise ℓ_2 loss values are also displayed.

Figure 6 Distributions of average ℓ_2 loss per scan evaluated on T1 slices with CDR $= 0/0.5/1/2$ reconstructed by: (**a**) MADGAN and (**b**) 7-SA MADGAN.

Figure 7 Distributions of average ℓ_2 loss per scan evaluated on T1c slices with no abnormal findings/brain metastases/various diseases reconstructed by: (**a**) MADGAN and (**b**) 7-SA MADGAN.

Figure 8 AUC performance on T1 scans using average ℓ_2 loss per scan under different training steps (i.e., 150k, 300k, 600k, 900k, 1.8M steps). Unchanged CDR $= 0$ (i.e., cognitively healthy population) is compared against: (**a**) all the other CDRs (i.e., dementia); (**b**) CDR $= 0.5$ (i.e., very mild dementia); (**c**) CDR $= 1$ (i.e., mild dementia); (**d**) CDR $= 2$ (i.e., moderate dementia).
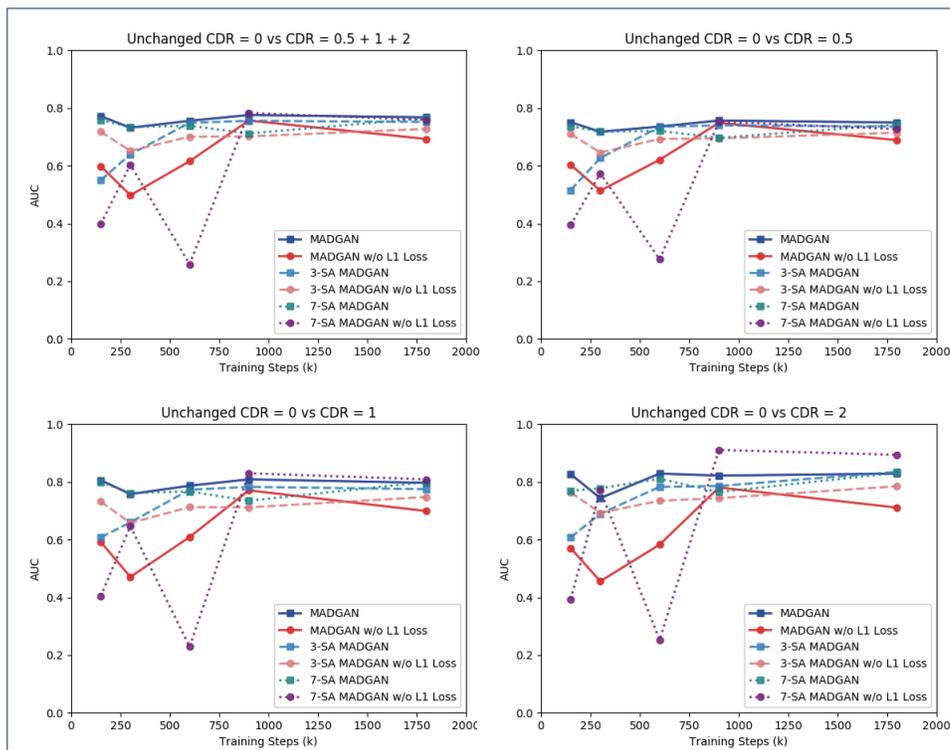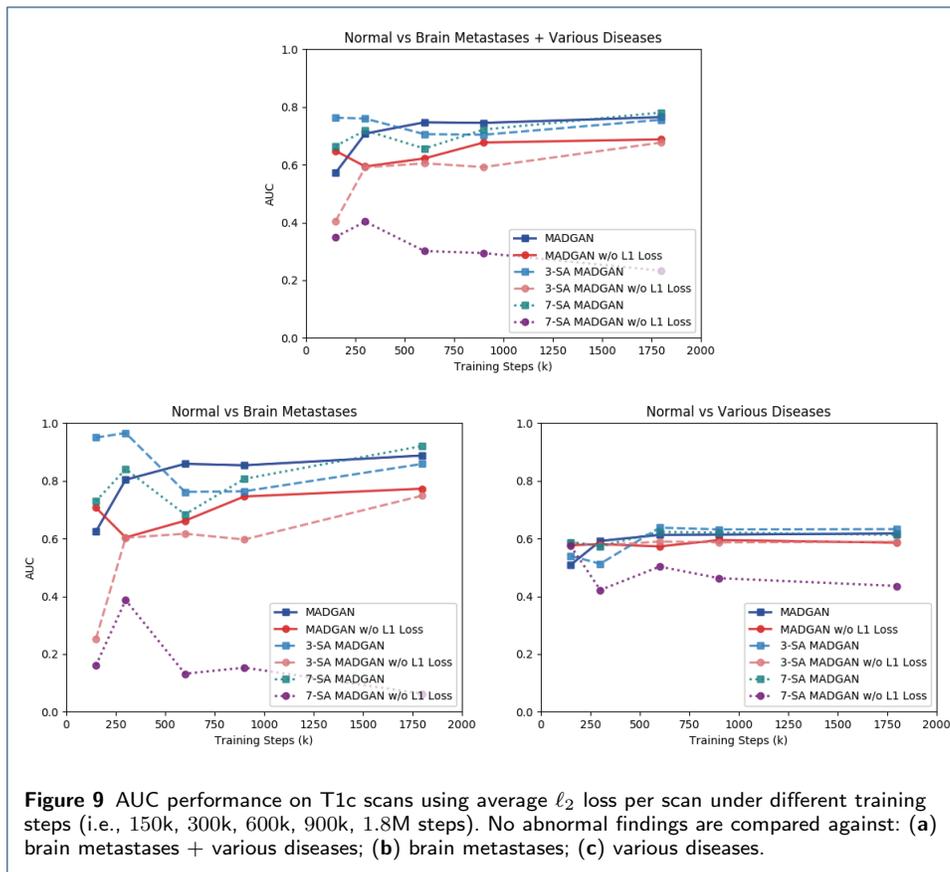
Figure 9 AUC performance on T1c scans using average ℓ_2 loss per scan under different training steps (i.e., 150k, 300k, 600k, 900k, 1.8M steps). No abnormal findings are compared against: (**a**) brain metastases + various diseases; (**b**) brain metastases; (**c**) various diseases.

Figure 10 Unsupervised anomaly detection results using average ℓ_2 loss per scan on reconstructed T1 slices (ROCs and AUCs). Unchanged CDR $= 0$ (i.e., cognitively healthy population) is compared against: (**a**) all the other CDRs (i.e., dementia); (**b**) CDR $= 0.5$ (i.e., very mild dementia); (**c**) CDR $= 1$ (i.e., mild dementia); (**d**) CDR $= 2$ (i.e., moderate dementia). Each model is trained for 1.8M steps.

Figure 11 Unsupervised anomaly detection results using average ℓ_2 loss per scan on reconstructed T1c slices (ROCs and AUCs). No abnormal findings are compared against: (**a**) brain metastases + various diseases; (**b**) brain metastases; (**c**) various diseases. Each model is trained for 1.8M steps.
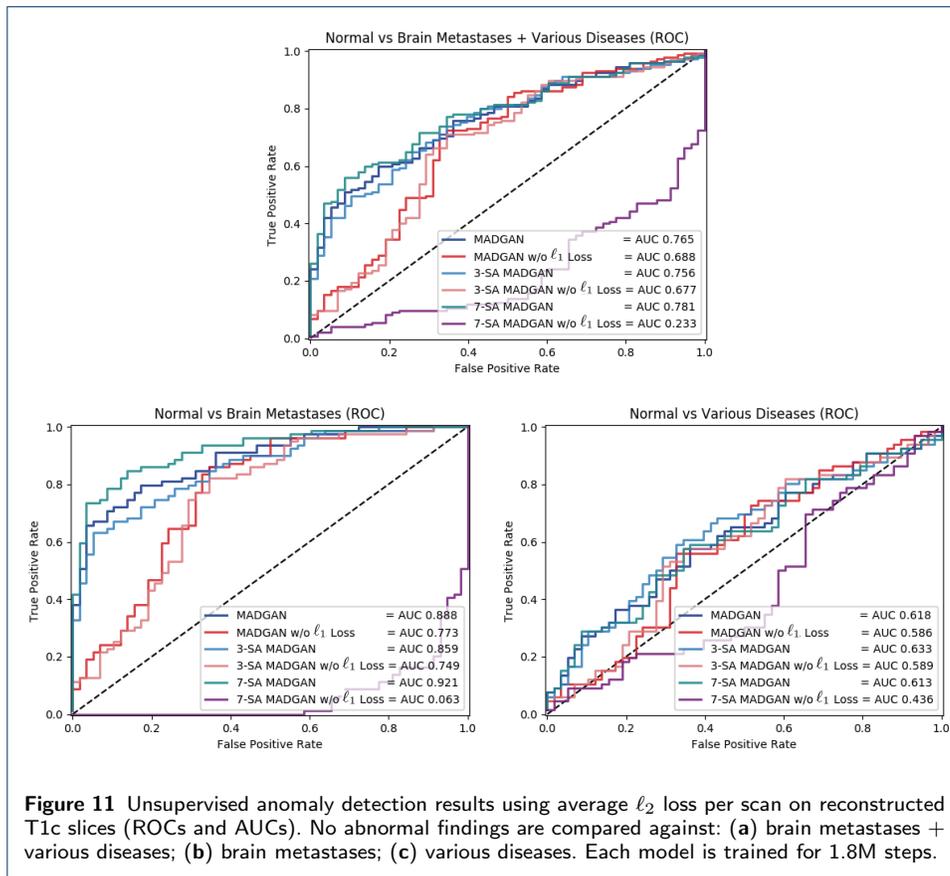
Table 1 AUC performance of unsupervised anomaly detection on T1 scans using average ℓ_2 loss (among whole slice sets/continuous 10 slice sets exhibiting the highest loss) per scan. Unchanged CDR $= 0$ (i.e., cognitively healthy population) is compared against: Unchanged CDR $= 0$ (i.e., cognitively healthy population) is compared against: (*i*) all the other CDRs (i.e., dementia); (*ii*) CDR $= 0.5$ (i.e., very mild dementia); (*iii*) CDR $= 1$ (i.e., mild dementia); (*iv*) CDR $= 2$ (i.e., moderate dementia). Each model is trained for 1.8M steps.

CDR $= 0$ vs	CDR $= 0.5 + 1 + 2$	CDR $= 0.5$	CDR $= 1$	CDR $= 2$
MADGAN	**0.768**	**0.750**	0.797	0.829
MADGAN (10 slice sets)	0.764	0.745	0.793	0.830
MADGAN w/o ℓ_1 Loss	0.693	0.689	0.699	0.711
MADGAN w/o ℓ_1 Loss (10 slice sets)	0.705	0.697	0.717	0.736
3-SA MADGAN	0.752	0.736	0.775	0.835
3-SA MADGAN (10 slice sets)	0.739	0.725	0.760	0.810
3-SA MADGAN w/o ℓ_1 Loss	0.728	0.715	0.748	0.785
3-SA MADGAN w/o ℓ_1 Loss (10 slice sets)	0.735	0.721	0.756	0.806
7-SA MADGAN	0.765	0.743	0.800	0.832
7-SA MADGAN (10 slice sets)	0.764	0.743	0.798	0.835
7-SA MADGAN w/o ℓ_1 Loss	0.759	0.727	**0.809**	**0.894**
7-SA MADGAN w/o ℓ_1 Loss (10 slice sets)	0.746	0.710	0.803	0.868

Table 2 AUC performance of unsupervised anomaly detection on T1c scans using average ℓ_2 loss (among whole slice sets/continuous 10 slice sets exhibiting the highest loss) per scan. No abnormal findings are compared against: (*i*) brain metastases + various diseases; (*ii*) brain metastases; (*iii*) various diseases. Each model is trained for 1.8M steps.

Normal vs	BM + VD	BM	VD
MADGAN	0.765	0.888	0.618
MADGAN (10 slice sets)	0.769	0.905	0.607
MADGAN w/o ℓ_1 Loss	0.688	0.773	0.586
MADGAN w/o ℓ_1 Loss (10 slice sets)	0.696	0.778	0.597
3-SA MADGAN	0.756	0.859	**0.633**
3-SA MADGAN (10 slice sets)	0.760	0.871	0.626
3-SA MADGAN w/o ℓ_1 Loss	0.677	0.749	0.589
3-SA MADGAN w/o ℓ_1 Loss (10 slice sets)	0.708	0.780	0.622
7-SA MADGAN	**0.781**	**0.921**	0.613
7-SA MADGAN (10 slice sets)	0.776	0.917	0.608
7-SA MADGAN w/o ℓ_1 Loss	0.233	0.063	0.436
7-SA MADGAN w/o ℓ_1 Loss (10 slice sets)	0.234	0.091	0.405